Available online at www.sciencedirect.com
ScienceDirect
Journal of Magnesium and Alloys xxx (xxxx) xxx
www.elsevier.com/locate/jma

Full Length Article

Additive friction stir deposition of AZ31B magnesium alloy

Sameehan S. Joshi[a,b], Shreyash M. Patil[a,b], Sangram Mazumder[a,b], Shashank Sharma[a,b], Daniel A. Riley[a,b], Shelden Dowden[b], Rajarshi Banerjee[a,b], Narendra B. Dahotre[a,b,*]

[a] Department of Materials Science and Engineering, University of North Texas, 3940 N Elm St, Denton, TX 76207, USA
[b] Center for Agile and Adaptive Additive Manufacturing, University of North Texas, 3940 N Elm St, Denton, TX 76207, USA

Received 5 December 2021; received in revised form 13 February 2022; accepted 31 March 2022
Available online xxx

Abstract

The current work explored additive friction stir deposition of AZ31B magnesium alloy with the aid of MELD® technology. AZ31B magnesium bar stock was fed through a hollow friction stir tool rotating at constant velocity of 400 rpm and translating at linear velocity varied from 4.2 to 6.3 mm/s. A single wall consisting of five layers with each layer of $140 \times 40 \times 1$ mm^3 dimensions was deposited under each processing condition. Microstructure, phase, and crystallographic texture evolutions as a function of additive friction stir deposition parameters were studied with the aid of scanning electron microscopy including electron back scatter diffraction and X-ray diffraction. Both feed material and additively produced samples consisted of the α-Mg phase. The additively produced samples exhibited a refined grain structure compared to the feed material. The feed material appeared to have a weak basal texture, while the additively produced samples experienced a strengthening of this basal texture. The additively produced samples showed a marginally higher hardness compared to the feed material. The current work provided a pathway for solid state additive manufacturing of Mg suitable for structural applications such as automotive components and consumable biomedical implants.

Keywords: Additive friction stir deposition; Magnesium alloys; Additive manufacturing; Thermomechanical processing; Materials processing; Solid state additive manufacturing.

1. Introduction

Magnesium (Mg) alloys are one of the lightest structural metallic materials with densities ~36% lower than the aluminum alloys [1–3]. The low density is also associated with their high specific strength and stiffness [4–6]. Mg alloys exhibit other attractive properties such as good electromagnetic shielding capability [7] and excellent biocompatibility due to non toxicity and modulus similar to the human bone [8,9]. Therefore, Mg alloys are suitable materials for application in various industries including aerospace, automotive, and biomedical. Apart from the efforts related to Mg alloy development, researchers have extensively explored advanced processing techniques for Mg alloys to enhance their formability, surface performance, and bulk properties [4,10,11]. These efforts have been extended into the newly emerging field of additive manufacturing (AM) of Mg alloys [12–14]. AM strategies for Mg alloys, which are still in their infancy, have focused on laser beam-based AM (LBAM) [15–17], wire arc AM (WAAM) [18,19], and friction stir AM (FSAM) [20–22]. The first two techniques are based on fusion of the feed material which is either powder or wire, whereas, the later is a solid state method. Out of these AM strategies, the FSAM based techniques provide unique advantages such as avoidance of powder which is especially crucial due to pyrophoric nature of Mg powder [23], ability to process commercially available feed material forms such as bars and chips [24], ease of fabrication of composite materials

* Corresponding author at: Center for Agile and Adaptive Additive Manufacturing, University of North Texas, 3940 N Elm St, Denton, TX 76207, USA.
E-mail address: Narendra.Dahotre@unt.edu (N.B. Dahotre).

https://doi.org/10.1016/j.jma.2022.03.011

Nomenclature

τ_{tool}	shear stress imparted by the tool (MPa)
$P_{actuator}$	pressure from actuator (N/mm^2)
ω	tool rotation speed (RPM)
V_{linear}	tool linear velocity (mm/s)
V_{feed}	deposition material feed rate (mm/s)
t_{tool}	tool residence time (s)
t_{feed}	feed material deposition time (s)
W_{tool}	tool wall thickness (mm)
R_{outer}	tool outer radius (mm)
R_{inner}	tool inner radius (mm)
H_{feed}	feed heat factor (W)
H_{tool}	tool heat factor (W)
Q_{feed}	input feed energy (J/mm^2)
Q_{tool}	input tool energy (J/mm^2)
Q_{total}	total input energy (J/mm^2)
A_{feed}	feed cross-section area (mm^2)
A_{tool}	tool cross-section area (mm^2)
k	thermal conductivity (W/m/K)
$T_{surface}$	temperature of deposition surface (°C)
$T_{thermocouple}$	temperature sensed by thermocouple (°C)
ΔX	distance between thermocouple bead and the location on the surface of deposited layer vertically above the thermocouple bead (mm)
$T_{average}$	average surface temperature (°C)
$t_{deposition}$	total deposition time (s)
$\dot{\epsilon}_{rotation}$	strain rate due tool rotation (/s)
$\dot{\epsilon}_{translation}$	strain rate due tool linear motion (/s)
$\dot{\epsilon}_{total}$	total strain rate (/s)
h	layer thickness (mm)
l	length travelled by feed material underneath the tool within the residence time (mm)
Z	Zener–Hollomon parameter ($10^{13} \times s^{-1}$)
$D_{recryst}$	recrystallized grain size (μm)
D_{afsd}	predicted grain size (μm)
$I_{(hkil)}$	experimentally measured peak intensity for a (hkil) reflection (arb units)
$I_{0(hkil)}$	intensity of the corresponding (hkil) reflection provided in ICDD JCPDS standard file for HCP α-magnesium (arb units)
n	grain growth exponent
k_0	grain growth equation constant
E	activation energy for Mg self lattice diffusion (kJ/mol)
R	universal gas constant (J/K/mol)

[21,22], and possibility of producing fully dense large scale components [25].

There are two main variants of FSAM: i) sheet-based FSAM where sheets of a material are joined or "added" together with the aid of a friction stir processing (FSP) tool and ii) AM fabrication via additive friction stir deposition (AFSD) where a hollow FSP tool is employed through which feed material is fed for subsequent deposition in solid state due to thermomechanical action between the tool and the feed material. AFSD has evolved recently with development of AM machines such as MELD®. AFSD further adds to the advantages of FSAM by enabling fabrication of large structures with relatively higher geometrical complexities [25–27]. AFSD has been explored for AM of conventional non-ferrous [28–31] and ferrous [32] alloys. One of the earliest papers demonstrated successful AFSD of aluminum 2024 alloy much before advent of MELD® technology [33]. However, there is a sparsity of research in open literature related to the AFSD of Mg alloys. To date, there is only one open document on AFSD of WE43 Mg alloy which is a master's degree thesis [34]. Although, the work presented by Calvert in this thesis provided a proof of concept for AFSD of Mg alloy, it lacked in correlation of the experimental findings to various process attributes. Understanding of the process attributes and their effects on the evolution of microstructure in the material is vital.

In view of the above discussion and limited literature on FSAM of Mg, the current work demonstrated successful solid state AM fabrication of AZ31B Mg alloy via AFSD. AZ31B Mg is one of the most commonly used structural Mg alloys in automotive and biomedical industries [4,8]. Extensive analysis of input AFSD parameters and corresponding logged data consisting of tool torque, actuator force, and thermocouple temperature was conducted. Multi-scale observations were performed on AFSD and feed material samples. The samples were observed using laser optical profilometry for surface characteristics. The microstructure, phase, and crystallographic texture evolutions in these samples were examined. Vickers hardness of the samples was measured in the cross-section. This research formed as a part of a decade long effort by the present group focusing on the advanced processing of Mg alloys [2,8,21,22,35–42]. It provided a successful pathway towards fabrication of Mg alloys using AFSD technique and methodology for realizing processing-structure-property relationships in AFSD produced materials.

2. Methods and materials

2.1. Additive friction stir deposition

Commercially available AZ31B Mg alloy (composition in wt.%: Mg-3Al-1Zn-0.5Mn) bar stock with cross-section of 9.5 × 9.5 mm^2 and 460 mm length was utilized during AFSD. The AFSD process was carried out using MELD® machine (schematic shown in Fig. 1(a)). The bar stock was fed into an actuator assembly of the machine through a hollow steel tool of 38.1 mm outer diameter, 118 mm height, and a coaxial square cavity of 9.5 × 9.5 mm^2 dimensions. AFSD experiments were performed on the AZ31B Mg base plate. The tool rotation speed (ω) was kept constant at 400 rpm and the tool linear velocity was varied in the range of 4.2 to 6.3 mm/s. The tool was shifted upward 1 mm at the end of deposition of each layer followed by deposition of a new layer on the top. Higher gap between the tool bottom surface and the

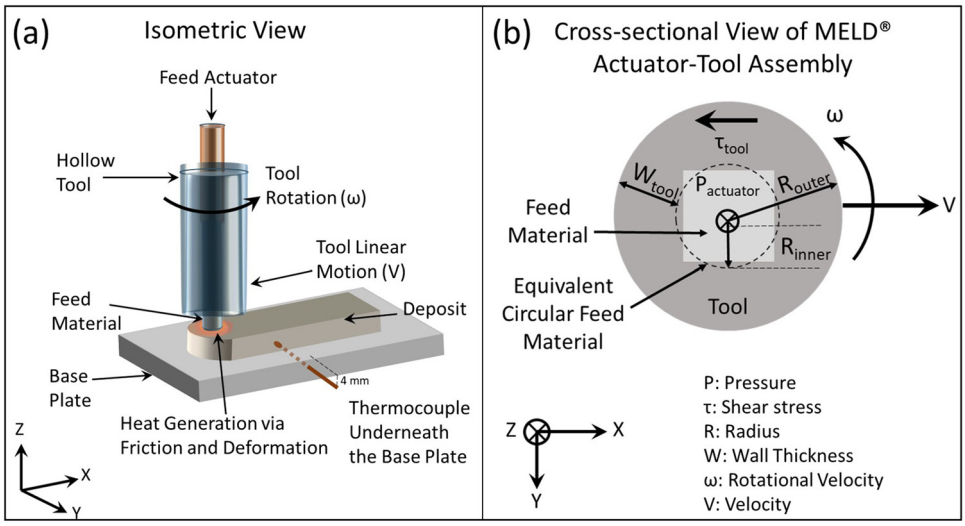

Fig. 1. Schematic illustrations of (a) AFSD process using MELD® machine and (b) cross-section view of MELD® actuator-tool assembly and associated process attributes.

Table 1
Process parameters utilized during AFSD of AZ31B Mg alloy .

Tool rotation speed, ω (RPM)	Tool linear velocity, V_{linear} (mm/s)	Deposition material feed rate, V_{feed} (mm/s)	Tool residence time, t_{tool} (s)	Feed material deposition time, t_{feed} (s)
400	4.2	2.1	9.0	2.5
400	5	2.5	7.6	2.1
400	6.3	3.2	6.0	1.7

base plate/deposited layer led to excessive flashing for AZ31B Mg. The tool residence time was estimated with the aid of following equation

$$t_{tool} = \frac{2 \times R_{outer}}{V_{linear}} \quad (1)$$

where t_{tool} is the tool residence time, R_{outer} is the tool outer radius (Fig. 1(b)), and V_{linear} is the tool linear velocity. Similarly, the feed material deposition time was estimated according Eq. (2). In this case, the radius of an equivalent circle having cross-sectional area same as the feed material was considered (Fig. 1(b)).

$$t_{feed} = \frac{2 \times R_{inner}}{V_{linear}} \quad (2)$$

where t_{feed} is the feed material deposition time, R_{inner} is the tool inner radius/equivalent circular feed material radius.

The intention of current work was to examine the effect of thermokinetics associated with various AFSD process parameters on microstructure evolution in the deposited material. The ratio between tool linear velocity (V_{linear}) and deposition material feed rate (V_{feed}) was maintained nearly same (~0.5) for each set of AFSD parameters to minimize generation of flash that eventually resulted in deposition of AZ31B Mg material with similar amount and thickness (~1 mm). The combination of process parameters (ω, V_{linear}, and V_{feed}) employed in the current work as listed in Table 1 provided a processing window for successful AFSD of AZ31B Mg with minimal flash. Furthermore, process data sets related to variation in tool torque and actuator force as a function of time were obtained form the onboard machine sensor log files. In addition, the temperature as a function of time was monitored during AFSD by a type *k* thermocouple located 4 mm underneath the base plate substrate (Fig. 1(a)). Omega multichannel digital data acquisition module was utilized for recording the thermocouple data. The temperature information was collected at a temporal resolution of 1 s.

2.2. Material characterization

Visual observations for the surface quality of the AFSD builds were conducted using laser confocal microscope (make Keyence vk6). Subsequently, the AFSD builds were separated from the base plate using wire electrical discharge machine (EDM). The samples were sectioned in the plane perpendicular to the tool travel direction (YZ plane in Fig. 1(a)) from the central location of the builds with the aid of a precision oil cooled slow speed ceramic wheel cutter. Phase evolution within the AFSD samples and feed material was examined with the aid of a Rigaku Ultima X-ray diffractometer equipped with Cu Kα radiation (wavelength: 0.1541 nm) operated at 40 kV. The step size was maintained at 0.5°/min and acquisition interval was 0.02°. The equipment set up and operating conditions were maintained constant during all the XRD runs and ensured containment of the X-ray beam within the sample cross-section area. The obtained X-ray diffraction (XRD) spectra were analyzed and indexed using Jade soft-

ware consisting of International Center for Diffraction Data (ICDD) files provided by Joint Committee of Powder Diffraction Standards (JCPDS).

Microstructure observations of the cross-sectional AFSD samples and feed material were conducted using scanning electron microscope (SEM) (FEI ESEM Quanta). Sample preparation consisted of mechanical polishing using 800–1200 grit SiC abrasive papers with ethanol as the lubricating medium. The mechanically ground samples were carefully washed with ethanol to remove any remnant SiC particles. The samples were then successively polished on a Buehler textmet cloth with diamond suspensions of 1 μm and 0.25 μm respectively. Final polishing was carried out on a Buehler chemomet cloth impregnated with colloidal silica suspension of particle size of 0.06 μm. The final polished samples were then gently lapped in ethanol on a clean Buehler texmet cloth rotated at low speeds to obtain a clean mirror finished surface. The prepared samples were then either subjected to etching in acetic picral (5 mL acetic acid + 6 g picric acid + 10 mL water in 100 mL ethanol) for ∼ 3 s for SEM and optical imaging or were immediately transferred to the SEM for electron back scatter diffraction (EBSD) analysis. The EBSD scans were conducted on a FEI Nova NanoSEM 230 equipment consisting of a Hikari super EBSD detector operated at 20 kV. A step size of 0.5 μm was employed during EBSD scans. Post EBSD data analysis was carried out on TSL OIM 8.0 analysis software to obtain inverse pole figure (IPF) maps and texture plots. The SEM, optical, and EBSD images were analyzed using ImageJ software to measure the grain sizes throughout the cross-section of the AFSD samples. At least 400 grains were measured in each sample to obtain a grain size distribution.

Vickers microhardnesses of the AFSD and the feed materials were measured using a Buehler Wilson tester. A normal load of 25 gf was applied for a dwell time of 10 s. Ten indentations were made across the cross-section of each sample to obtain average hardness value and corresponding standard deviation in accordance with the ASTM E384 standard [43]. The intention of this preliminary work was to probe global and average properties of the deposits.

3. Results and discussion

As a first step of the analysis, to realize the collective effect of tool-feed material-base plate/deposited layer interactions during the AFSD fabrication, the process attributes were monitored by the onboard sensors. These attributes helped in estimating the heat components associated with the tool and the deposition feed material which contributed to plasticization and deposition of AZ31B Mg. Moreover, the heat components were further converted into the average areal energy input and correlated with the microstructure evolution as elaborated in the following subsections.

3.1. Recorded process attributes

The values of tool torque and feed actuator force collected by the onboard machine sensors were extracted and expressed as a function of time for various AFSD conditions (Fig. 2). There was a built up in tool torque during plasticization phase until the deposition began (Fig. 2(a)). During the multi layer deposition process, the average tool torque decreased. The AFSD process carried out with highest tool linear velocity of 6.3 mm/s exhibited highest overall tool torque compared to the other two tool linear velocities of 5.0 and 4.2 mm/s (Fig. 2(a)). The actuator force for AFSD conditions corresponding to 5.0 and 6.3 mm/s tool linear velocities experienced an increase at the beginning of the AFSD process followed by a decrease (Fig. 2(b)). On the other hand, the actuator force for AFSD condition corresponding to tool linear velocity of 4.2 mm/s took relatively longer time to increase and thereafter remained at higher values compared to the other two higher tool linear velocities (Fig. 2(b)). For this particular condition, it was observed during the AFSD experiment that a relatively high amount material removal through flash formation occurred compared to the other process conditions. Therefore, higher actuator force was imparted by the machine to maintain the feed rate of 2.1 mm/s while filling the gaps formed due to flash ejection in the previously deposited material. As a result, an uptake in actuator force was observed after ∼80 s into the AFSD process carried out with the tool linear velocity of 4.2 mm/s. Both the tool torque and actuator force are reflective of the deformation behavior of the AZ31B Mg while undergoing AFSD process. The activation of multiple competing slip systems at various times during such a high temperature severe plastic deformation is likely to influence the required tool torque and actuator force to carry out the successful shearing and deposition of the material during the AFSD process.

In addition to the tool torque and the actuator force, the temperature recorded by type k thermocouple was expressed as a function of time (Fig. 3(a)–(c)). In all the cases, there appeared to be a rise in the maximum and the minimum temperatures experienced by the thermocouple when first two layers were deposited (maximum temperature ranges 378–410 °C and 387–406 °C and minimum temperature ranges 202–224 °C and 206–228 °C for tool linear velocity range of 4.2–6.3 mm/s) followed by a slight decease in the maximum temperate and slight increase in the minimum temperature for the subsequent layers (maximum temperature ranges 401–363 °C and 402–390 °C and minimum temperature ranges 227–228 °C and 241–266 °C for tool linear velocity range of 4.2–6.3 mm/s). During deposition of the first layer, the feed material was rotated against the base plate at room temperature. There was a built up of heat due to plasticization of the feed material and surface/sub-surface region of the base plate at the interface between the feed material and the base plate as well as the friction between tool/feed material against the base plate at the room temperature. On the other hand, during the deposition of the subsequent layers, the previously deposited layer or layers that remained at elevated temperature served as a build surface. This led to a rise in maximum and minimum temperatures observed from layer 1 to layer 2 even though the distance between thermocouple and the location of material deposition increased with added layers

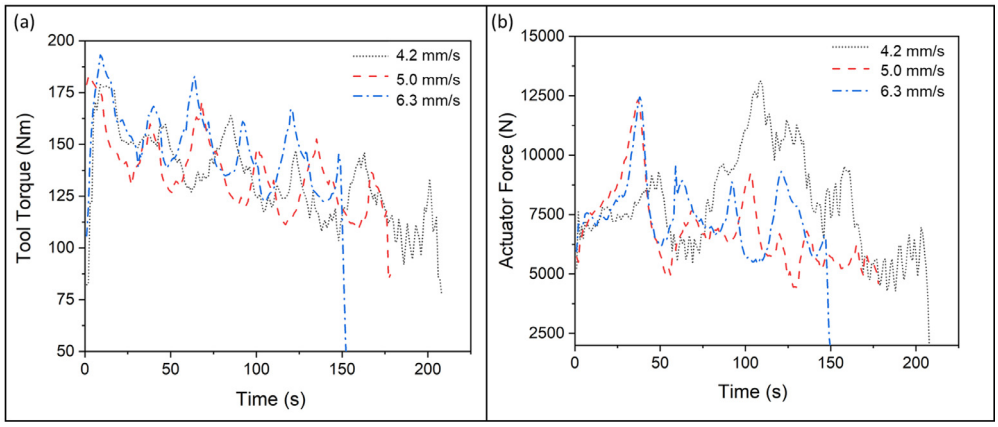

Fig. 2. Variation in (a) tool torque and (b) actuator force during AFSD as a function of time for various tool linear velocities.

Table 2
Various physical process attributes generated during the AFSD process.

Tool linear velocity, V_{linear} (mm/s)	Deposition material feed rate, V_{feed} (mm/s)	Shear stress imparted by tool, τ_{tool} (N/mm^2)	Feed material pressure, P_{feed} (N/mm^2)	Feed heat factor, H_{feed} (W)	Tool heat factor, H_{tool} (W)	Input tool energy, Q_{tool} (J/mm^2)	Input feed energy, Q_{feed} (J/mm^2)	Total input energy, Q_{total} (J/mm^2)
4.2	2.1	11.7	81.2	290	6990	107.4	8.6	116
5	2.5	12.0	73.8	263	7148	91.8	6.2	98
6.3	3.2	12.7	72.6	259	7572	77.6	4.4	82

(Fig. 3). Although the maximum thermocouple temperatures continued to slightly decrease after third layer onward due to the increasing distance between the thermocouple and the location of the deposited layers, the minimum temperatures continued to increase slightly due to the heat build up in the deposited volume (Fig. 3).

The recorded process data sets of tool torque, actuator force, and thermocouple temperature during each AFSD run were considered to estimate the average areal energy input and surface temperature during deposition of each layer.

3.1.1. Effect of process attributes on energy inputs

The forces experienced by the tool and feed material while in simultaneous rotation-translation motion lead to the friction between tool/feed material-base plate. In order to estimate the average input energy during AFSD process, the average values of tool torque (132–143 Nm for corresponding tool linear velocity range of 4.2–6.3 mm/s) and actuator force (7871–6590 N for corresponding deposition material feed rate of 2.2–3.2 mm/s) were extracted from the recorded data (Fig. 2) for the entire deposition cycle under various AFSD conditions. The average values of tool torque were converted into corresponding force based on the tool radius (Tool force = Tool torque /R_{outer}). The force data from tool was converted into the shear stress (τ) (Shear stress = $\frac{Shearforce}{Area}$) imparted by the tool onto spreading material underneath the tool surface. Further, the actuator force was translated into pressure (P) component based on the area of the tool and equivalent circular area for the feed material respectively (Fig. 1 and Table 2). These shear and pressure components were then translated into heat factors from the tool and feed as expressed in Eqs. (3) and (4) respectively [44,45]

$$H_{tool} = \frac{4\pi^2}{3}\omega\tau_{tool}\ (R_{outer}^3 - R_{inner}^3) \tag{3}$$

$$H_{feed} = \frac{4\pi^2}{3}\mu\omega P_{feed}\ (R_{inner}^3 - 3R_{inner}^2.h) \tag{4}$$

where H_{tool} and H_{feed} are the heat factors (W) from the tool and the feed respectively (Table 2), ω is the rotational speed of the tool (hertz) , τ_{tool} is the shear stress imparted by the tool on the feed material spreading underneath, μ is coefficient of friction between AZ31B Mg and the tool steel, the value of which has been reported as 0.6 [46], P_{feed} is the pressure on the feed rod from the actuator (Table 2), and h as explained earlier is the feed material layer thickness of ~1 mm being deposited outside the hollow tool. The values of computed heat factors from the tool and the feed material are listed in Table 2. The heat factors associated with the tool were ~25 times higher than the heat factors associated with the feed and decreased as a function of tool linear velocity (Table 2). The heat factor for feed material decreased as a function of tool linear velocity (Table 2). The tool heat factors were mainly dependent on the torque experienced by the tool during the AFSD. The tool torque increased as a function of the tool linear velocity leading to a corresponding increase in the tool heat factor as a function of tool linear velocity (Fig. 2(a) and Table 2). Similar findings related to relation of torque with tool linear velocity were noted in the literature [47,48]. The heat factors associated with the feed material were driven by the normal actuator force experienced by the material under-

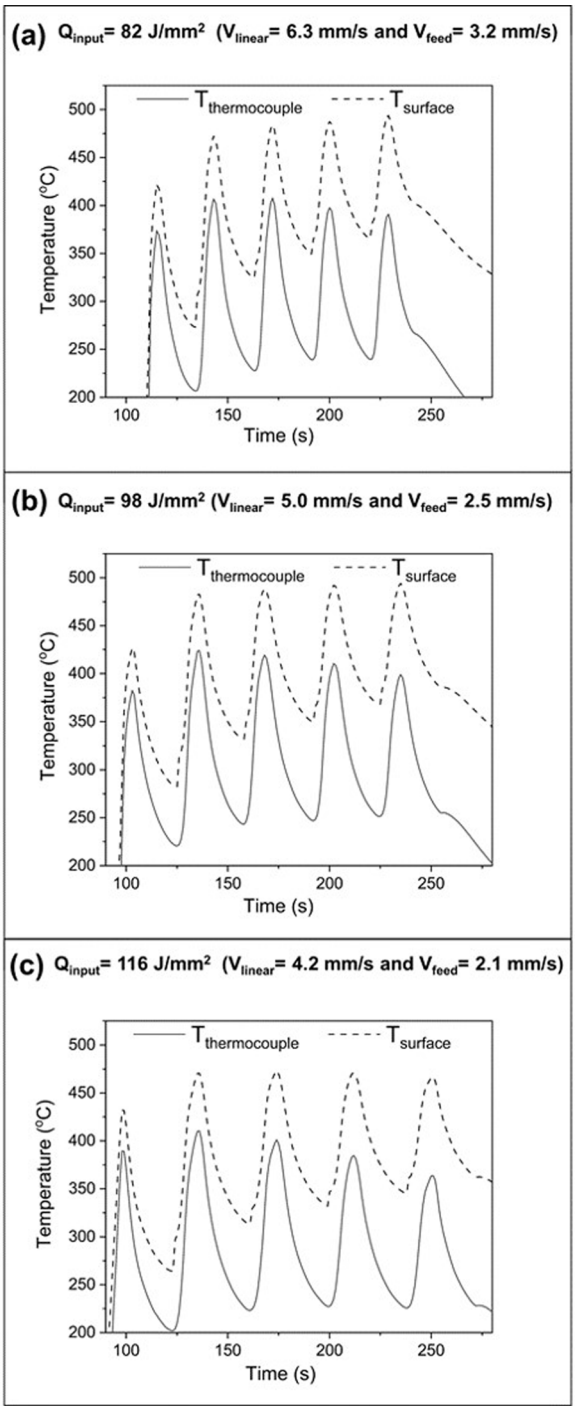

Fig. 3. Set of plots showing thermocouple based temperature measurement as a function of time at the center of the AFSD track 4 mm below the AZ31B Mg base plate for total input energy conditions corresponding to (a) 82 J/mm^2, (b) 98 J/mm^2, and (c) 116 J/mm^2. The variations in predicted surface temperatures using the Fourier's law for each AFSD condition are also plotted.

going AFSD. The average actuator force decreased as a function of tool linear velocity, therefore, reducing the heat factor associated with the feed material (Fig. 2(b) and Table 2).

The heat input then was converted in to energy input per unit area for the feed material and the tool as expressed in Eqs. (5) and (6)

$$Q_{tool} = \frac{H_{tool}.t_{tool}}{A_{tool}} \tag{5}$$

$$Q_{feed} = \frac{H_{feed}.t_{feed}}{A_{feed}} \tag{6}$$

where Q_{tool} and Q_{feed} are the energy inputs per unit area (J/mm^2) for the tool and the feed respectively and A is the area of the heat source. Finally, the total input energy during AFSD process was calculated according to Eq. (7)

$$Q_{total} = Q_{feed} + Q_{tool} \tag{7}$$

The values of energy inputs from the tool and the feed material along with their summation as total energy input are listed in Table 2 and plotted as a function of linear tool velocity (V_{linear}) and feed material rate (V_{feed}) in Fig. 4. These values decreased with an increase in the linear tool velocity and deposition material feed rate. Major contribution to the total energy input was from the tool. The energy inputs associated with the tool (Q_{tool}) and the feed material (Q_{feed}) were directly proportional to the residence/deposition time and inversely proportional to the respective areas of the heat sources (Eqs. (5) and (6)). The residence/deposition time associated with the tool (t_{tool}) and the feed (t_{feed}) decreased with an increase in the tool linear velocity, thus, reducing the total input energy (Q_{input}) as a function of tool linear velocity (V_{linear}) (Table 1). Furthermore, the effective tool area was ~7 times larger compared to the feed material. Therefore,although the energy input imparted by the tool correspondingly scaled down, it remained ~15 times higher than the energy input from the feed. Due to the combination of various physical attributes discussed here, the estimations as per Eq. (7) indicated a decrease in the total input energy (Q_{total}) (J/mm^2) as a function of tool linear velocity (Fig. 4).

3.1.2. Estimation of surface temperatures during AFSD process

With the aid if the heat factors computed from Eqs. (3) and (4) along with the temperature data recorded by the thermocouple during the AFSD process (Fig. 3), the evolution of surface temperature due to combined interaction of tool and feed material with the deposited layer was predicted based on Fourier's law of heat conduction as expressed in the following equation

$$H_{tool} + H_{feed} = -kA\left[\frac{T_{Surface} - T_{Thermocouple}}{\Delta X}\right] \tag{8}$$

where k is the temperature dependent thermal conductivity provided in the literature [49], A is the total area of contact of the tool (A_{tool}) and the feed material (A_{feed}) with the deposit/base plate, $T_{Surface}$ is the temperature to be predicted, $T_{Thermocouple}$ is the temperature recorded by thermocouple, and ΔX is the distance between thermocouple bead and the location on the surface of deposited layer vertically above the thermocouple bead. The surface temperature at the locations vertically above the thermocouple bead similar to the first layer

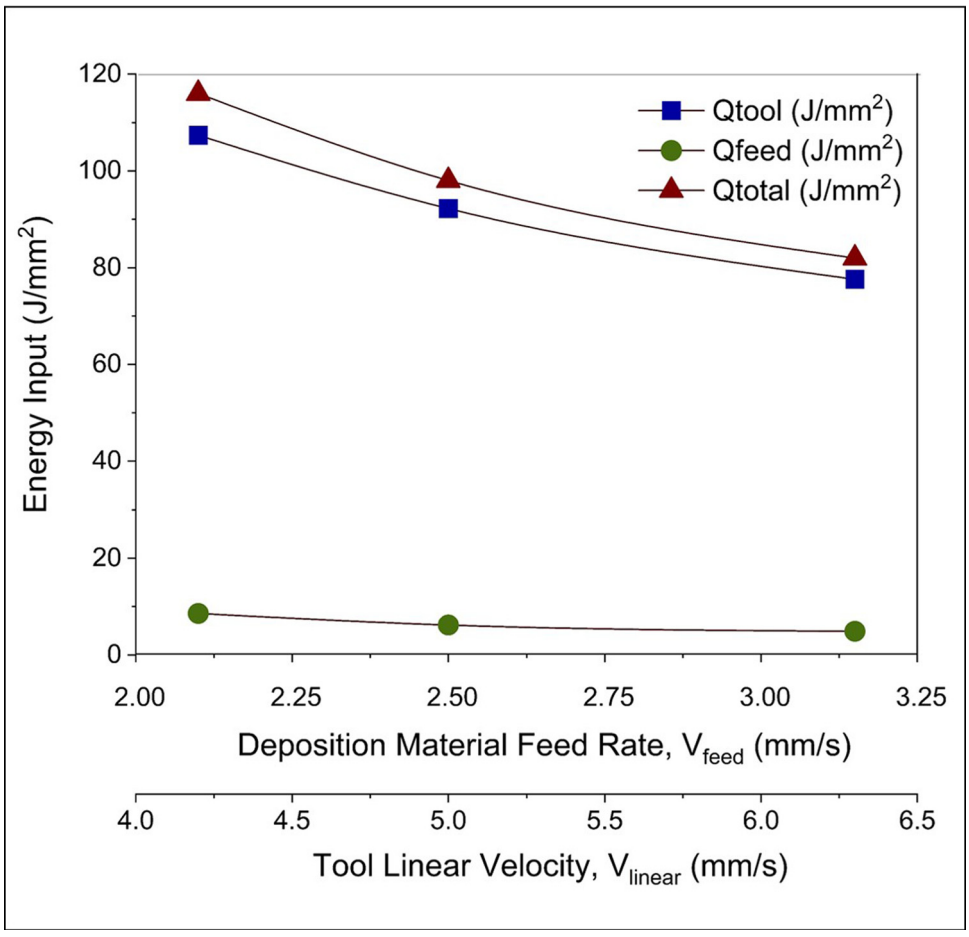

Fig. 4. Calculated average energy input associated with the tool and feed material, and corresponding total energy input as function of process parameters during AFSD of AZ31B Mg.

Table 3
Predicted physical parameters and grain sizes for AFSD process .

Total energy input, Q_{total} (J/mm^2)	Average surface temperature, $T_{average}$ (C°)	Total deposition time, $t_{deposition}$ (s)	Total strain rate, $\dot{\epsilon}_{total}$ (s^{-1})	Zener–Hollomon parameter, Z ($10^{13} \times s^{-1}$)	Recrystallized grain size, $D_{recryst}$ (μm)	Final predicted grain size, D_{afsd} for $n = 2.5$ (μm)	Final predicted grain size, D_{afsd} for $n = 2.9$ (μm)
82	390.7	130	512.16	2.1	2.0	6.0	31.1
98	388.9	155	512.13	2.3	1.9	6.3	32.3
116	370.5	185	512.11	4.6	1.6	5.1	27

was estimated for each layer for a given AFSD condition and plotted in Fig. 3. During these temperature calculations, as an assumption, the radiative heat losses from the surface region during the deposition process were not considered. The temporal evolution of estimated temperature followed the same trend as that of temporal variation of temperature recorded by the thermocouple (Fig. 3). The estimated surface temperature increased from layer 1 to layer 2 and then appeared to reach a stable value for each AFSD condition. Furthermore, the surface peak temperatures were higher by ~30 to 100 °C compared to the peak temperatures sensed by the thermocouple and estimated average surface temperature ranged from 370.5 to 390.7 °C (Table 3). The predicted surface temperatures were relatively lower for AFSD sample corresponding to 116 J/mm^2 compared to the other two lower input energy conditions. As mentioned earlier, this particular AFSD condition experienced relatively highest amount of material ejection via flash formation among the process conditions employed in the current work. Therefore, the heat input for this particular condition was partially dissipated through material deformation via flash rather than the layer deposition.

With this examination of various process attributes, estimated total energy input, and predicted surface temperature during the AFSD process, the AFSD fabricated AZ31B Mg samples were evaluated for the structure-property evolution. As the initial step, the AFSD AZ31B Mg samples were visually observed and surface characteristics were recorded.

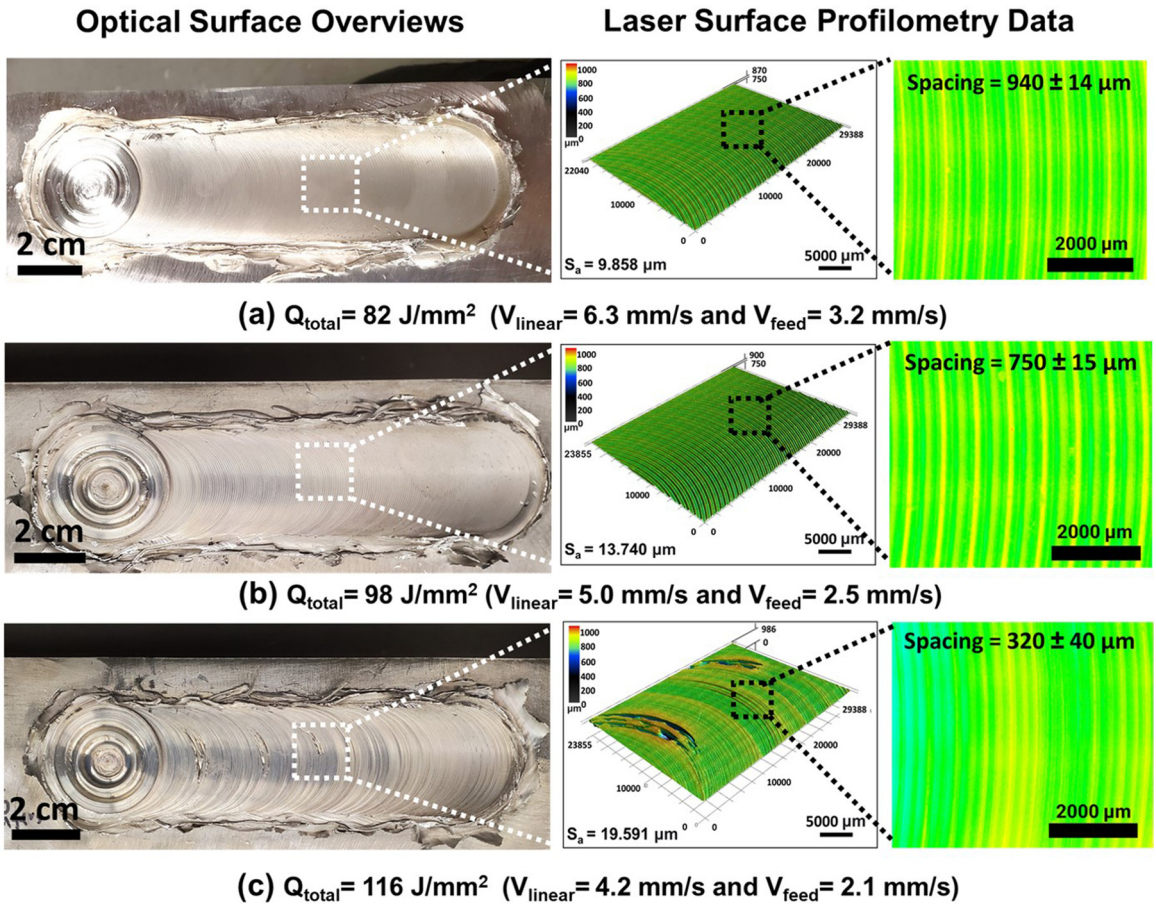

Fig. 5. Optical overviews of AFSD AZ31B Mg samples and corresponding laser optical surface profilometry images revealing the areal surface roughness values and spacing between the ripple marks. (a) Q_{total} = 82 J/mm^2, (b) Q_{total} = 98 J/mm^2, and (c) Q_{total} = 116 J/mm^2.

3.2. Surface characteristics

As a first level of analysis, the deposited samples were subjected to visual examination under the laser confocal microscope (Fig. 5(a)–(c)). The sample thicknesses were measured as 4.2, 4.15, and 4.3 corresponding to the total energy input of 82, 98, and 116 J/mm^2 respectively. During AFSD, the first layer was deposited on the base plate while the previously deposited layer served as the base for subsequent layer. Although, majority of the high actuator force (Fig. 2(b)) was expended in deformation and subsequent deposition of the feed material on the base plate/previous layer, it is likely that the previous layer was also partially deformed in surface/subsurface region due to the inherent nature of the process (transfer of part of the axial force through deformed feed material). However, if not impossible, it was experimentally difficult to probe in-situ manner the extent and spatial distribution of such partial deformation of a previous layer while serving as a base for the subsequent layer deposition. During such surface/sub-surface deformation of the material being deposited and the prior layer/base plate, portion of the material was ejected through the mode of flash formation around the edges of deposit. Thus, although the stand-off distance between the tool and the base plate was maintained at 1 mm and tool was shifted upwards by 1 mm at the end of each layer followed by deposition of a new layer, the deposited layer had thickness reduced by ∼150 µm.

The surfaces of all samples possessed concentric ripple marks that were generated due to simultaneous rotational and translation motion of the tool. These ripple marks were spaced at distance of 940 ± 14 µm for 82 J/mm^2, 750 ± 14 µm for 98 J/mm^2, and 320 ± 40 µm for 116 J/mm^2 resulting in average surface roughness (S_a) of 9.858 µm, 13.740 µm, and 19.591 µm respectively (Fig. 5). The ripple formation is attributed to the mechanism of plasticized material transfer from the feed stock that is attached to the rotating tool due to the shear force experienced at the interface by the relative motion of the base plate/layer. Generation of frictional heat and heat concentration at the contact between the tool and the base plate/deposited layer during AFSD caused reduction in flow stress of the feed material thereby resulting in severe plastic deformation in the form of ripples.

During AFSD process, the tool was positioned at the constant distance (∼1 mm) from the substrate (base plate and/or

previously deposited layer). Hence, it was reasonable to assume that the average layer thickness and average mass deposited remained same throughout the process. Furthermore, the area of hollow tool through which the feed material was delivered in contact with the substrate and its rotational velocity was constant. In light of this, the flow stress remained directly proportional to the linear velocity and the residence/contact time of the tool. In present work, linear velocity was varied from 4.2 mm/s to 6.3 mm/s thereby varying the residence time from 9.0 to 6.0 s. Such dependence of the flow stress driven deformation on the tool linear velocity manifested into evolution of characteristic surface ripples with variable spacial distance between them and average surface roughness (Fig. 5). Minor physical defects (porosities) were observed on the surface of the AFSD samples corresponding to the lowest linear velocity of 4.2 mm/s (116 J/mm^2). Such defects plausibly arose due to higher total energy input which likely led to localized joining of the feed material to the tool and its eventual removal as flash instead of shearing and deposition [50].

3.3. Microstructure, phase, and crystallographic texture evolution

Preliminary examination of phases present in the feed material and phase evolution within the AFSD samples by XRD suggested presence of α-Mg HCP phase in both the cases (Fig. 6). Interestingly, the intensity of $(10\bar{1}1)$ pyramidal peak dropped significantly for AFSD samples compared to the feed material (Fig. 6). Correspondingly there was an increase in the peak intensity of the primary $(10\bar{1}0)$ and secondary $(11\bar{2}0)$ prismatic planes for the AFSD samples compared to the feed material (Fig. 6). Considering that the experimental as well as sampling conditions were maintained constant during each XRD run and the XRD spectra were plotted at same X and Y axis scales, possibly the change in peak intensities could be attributed to changes in the fraction of specific crystallographic planes lying parallel to the $Y-Z$ sample plane.

To quantify the intensity variation corresponding to various crystallographic reflections in AFSD samples and the feed material, intensity ratios were computed according to Eq. (9) [51,52]

$$Intensity\ Ratio = \frac{I_{(hkil)}}{I_{0(hkil)}}\left[\frac{1}{n'}\sum\frac{I_{(hkil)}}{I_{0(hkil)}}\right]^{-1} \quad (9)$$

where I_{hkil} is an experimentally measured peak intensity for a (hkil) reflection, $I_{o(hkil)}$ is a intensity of the corresponding (hkil) reflection provided in ICDD JCPDS standard file for HCP α magnesium (file number 00-004-0770), and n' is the number of reflections (in present case 10) considered for calculation from a given spectrum.

Intensity ratios for all the peaks were computed as per Eq. (9) and select intensity ratios for $(10\bar{1}0)_{prismatic}$, $(10\bar{1}1)_{pyramidal}$, $(11\bar{2}0)_{prismatic}$, and $(20\bar{2}1)_{pyramidal}$ reflections were expressed as a function of total input energy (Q_{total}), tool linear velocity (V_{linear}), and deposition material feed rate (V_{feed}) (Fig. 7). The intensity ratios of the feed material indicated a random distribution of crystallographic planes. For the AFSD samples, the intensity ratios for prismatic planes increased initially by nearly two and half folds for the lowest total input energy condition of 82 J/mm^2 when compared to the feed material (Fig. 7). With further increase in input energy, the AFSD samples showed a marginal reduction in intensity ratios of the prismatic planes. On the contrary, the intensity ratios for the pyramidal reflections corresponding to AFSD samples experienced an initial steep decrease followed by a marginal increase as a function of total input energy (Fig. 7). These observations suggested that AFSD samples had a pronounced increase in the density of prismatic planes lying parallel to the YZ plane (Fig. 1). The reasons behind such a distinct increase in the fraction of prismatic planes in the YZ plane of the AFSD samples can be attributed to the development of a basal {0001} texture which has been more conclusively established in the SEM-EBSD analysis presented subsequently in this paper. With this preliminary idea about the phase evolution and variation in intensity ratios of crystallographic reflections with respect to the process parameters in the AFSD AZ31B Mg, the microstructures of these samples were observed.

SEM observations on feed material and AFSD AZ31B Mg samples suggested presence of equiaxed grains of α-Mg (Fig. 8). The feed stock appeared to have a wide grain size distribution with an average grain size of 13.5 μm, with some of the larger grains in the regime of 50–60 μm (Fig. 8(a)). The grain size shifted to a finer distribution for AFSD samples as compared to the feed material (Fig. 8(b)–(d)). For the lowest total input energy (Q_{total}) samples corresponding to 82 J/mm^2, the grain size distribution appeared to spread over very narrow range of finer grains (< 5 μm) with an average grain size of 5.0 μm (Fig. 8(b)). With an increase in the total input energy to 98 J/mm^2 (average grain size of 5.2 μm) and 116 J/mm^2 (average grain size of 6.0 μm), the proportion of fine grains (< 5 μm) reduced even further along with the existence of lower proportion of larger grains (5–35 μm) (Fig. 8(c) and (d)). These observations suggested that the feed material likely underwent dynamic recrystallization during AFSD. Moreover, the recrystallized grains plausibly commenced the growth process due to the thermal exposure experienced as a result of reheating within the same layer and during deposition of additional layers.

The grain size evolution described above during AFSD process is a resultant of thermomechanical nature of the process. Such thermomechanical effect can be correlated to the strain rate associated with the AFSD process that in turn is affected due to combined rotation and translation motion of the tool and feed material. The feed material thickness outside of the hollow cavity experienced simultaneous softening/deformation and spreading due to frictional heat and forces generated during AFSD. Based on the simultaneous occurrence of these complex physical phenomena and considering that only the tool linear velocity was varied during the experiments keeping all other process parameters as constant, the total strain rate was approximately expressed according to

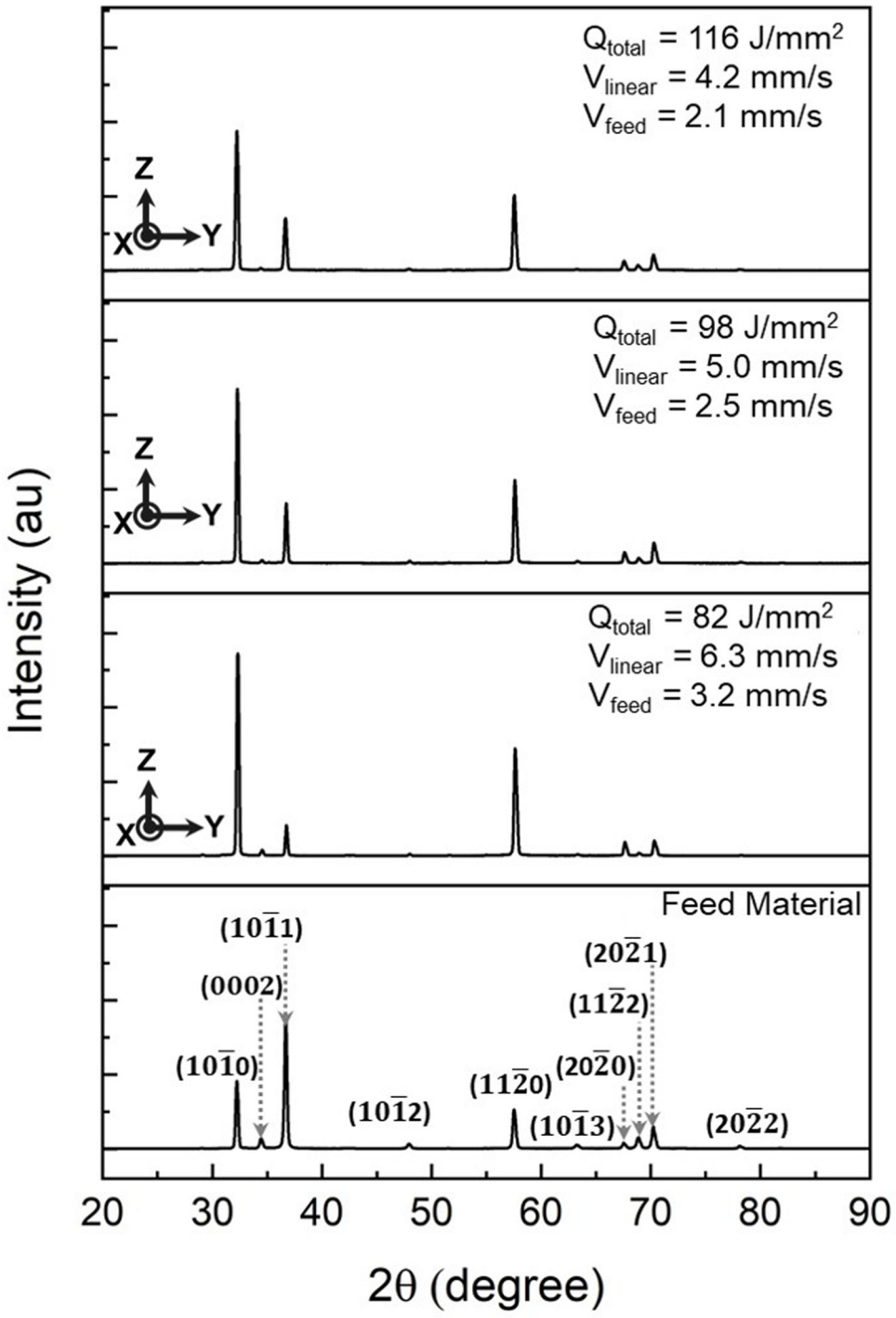

Fig. 6. XRD spectra in *YZ* plane for the feed material and AFSD AZ31B Mg samples.

the following equation.

$$\dot{\epsilon_{total}} = \dot{\epsilon}_{rotation} + \dot{\epsilon}_{translation} \tag{10}$$

where $\dot{\epsilon}_{rotation}$ and $\dot{\epsilon}_{translation}$ are the strain rates associated with rotational and linear motion of tool respectively and $\dot{\epsilon}_{total}$ is the summation of rotational and translation strain rates. The strain rate associated with the rotational motion of the tool is expressed according to the Eq. (11) [53–56]

$$\dot{\epsilon}_{rotation} = \frac{2\pi R_{tool}\frac{\omega}{2}}{h} \tag{11}$$

Whereas, the strain associated due to transnational motion of the tool is expressed as

$$\dot{\epsilon}_{translation} = \frac{V_{linear}}{l} \tag{12}$$

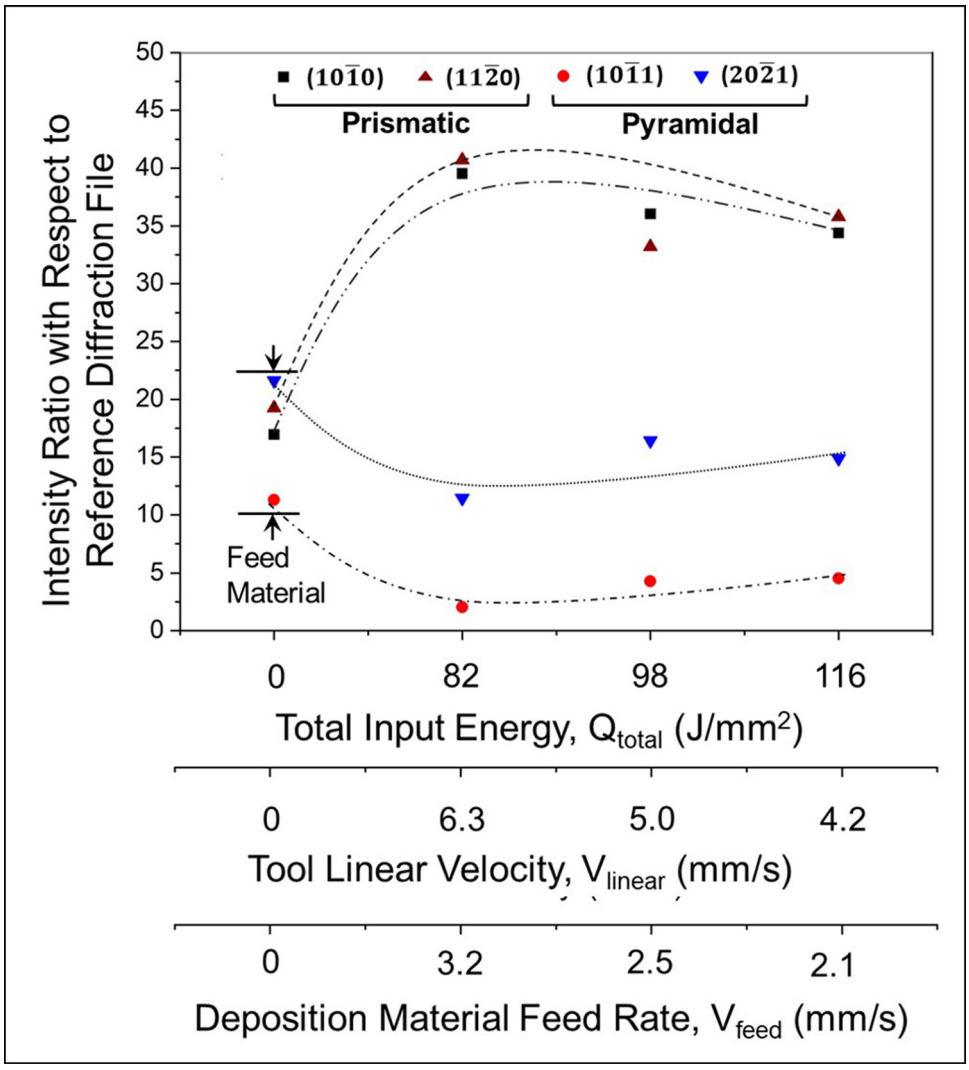

Fig. 7. Evolution of intensity ratios corresponding to select prismatic and pyramidal atomic plane reflections as a function process parameters during AFSD of AZ31B Mg.

where l is the length traveled by the feed material underneath the tool while being deformed/sheared within the residence time for a given tool linear velocity. In present case, upper bound of such a characteristic l was considered equal to the tool diameter. The values of total predicted strain rates (ϵ_{total}) are presented in Table 3. It appeared that, the change in linear velocity made minor differences in the total strain rate for the range of linear velocities of the present work. Furthermore, within the range of linear velocities (V_{linear}) (4.2–6.3 mm/s) employed in the present work, the predicted total strain rate (ϵ_{total}) appeared to vary marginally (Table 3). However, the manifestation of influence of the AFSD process variables (linear velocity and total input energy) on deformation characteristics, as described earlier, is evident in the surface morphologies (roughness and ripple marks). On the contrary, the strain rate is likely to influence dynamic recrystallization and thermal assisted grain growth. These effects are discussed below.

The Zener–Hollomon parameter which couples strain rate and temperature effects towards deformation characteristics was extracted from the strain as follows using the overall average surface temperature for each condition [1,53,57–60].

$$Z = \dot{\epsilon_{total}} exp\left[\frac{E}{RT_{Surface\ Average}}\right] \tag{13}$$

where Z is the Zener–Hollomon parameter, E is the activation energy for Mg self lattice diffusion (135 kJ/mol) [61,62], R is the universal gas constant (8.314 J/K/mol). The estimated values of Z are listed in Table 3. The Z parameter was utilized to predict the recrystallized grain size which evolves during a single pass deposit of AFSD without any influence of the reheating effects using the following equation [53]

$$lnD_{recryst} = 9 - 0.27lnZ \tag{14}$$

where $D_{recryst}$ is the recrystallized grain size within the AFSD deposit in μm. The computed values of $D_{recryst}$ were in the range of 1.6 to 2.0 μm for the input energy range of 82 to 116 J/mm^2 (Table 3). These predictions suggested that the combination of temperature and the strain rate led to recrystallization of the severely deformed feed material leading to

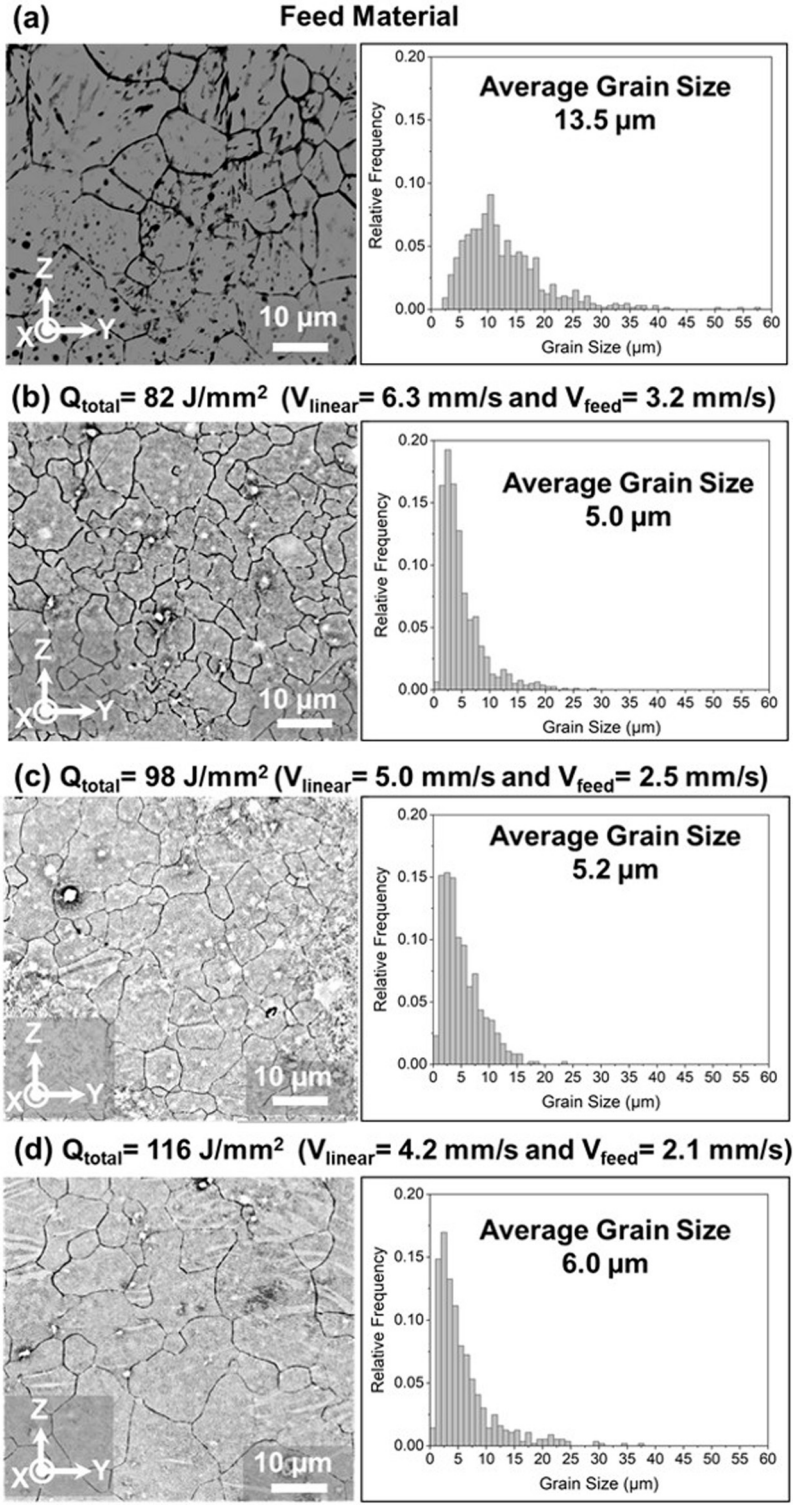

Fig. 8. SEM micrographs and grains size distribution plots corresponding to (a) feed material and AFSD AZ31B Mg samples deposited with (b) Q_{total} = 82 J/mm^2, (c) Q_{total} = 98 J/mm^2, and (d) Q_{total} = 116 J/mm^2.

a fine grain size in freshly deposited AZ31B Mg. However, the microscopy observation suggested that the grain size distribution in the AFSD samples was relatively wider with majority of the grains in the range of 0–10 µm along with few grains as large as 30–35 µm at the far end of the distribution (Fig. 8 (b)–(d)). This indicated that the recrystallized grains experienced growth due to in-layer reheating effects as well as reheating due to subsequently added layers. The following

equation was employed to predict such grain growth [63]

$$D^n_{AFSD} - D^n_{recryst} = k_0 exp\left[\frac{-E}{RT_{Surface\ Average}}\right]t \quad (15)$$

where D_{AFSD} is the final grain size in multi layered AFSD deposits, n is the grain growth exponent, k_0 is a constant = 2.75×10^{-5} [61,63], t is the total time of deposition extracted from the thermocouple data (Fig. 3 and Table 3). Generally, the value of n is obtained for isothermal grain growth studies by monitoring the grain size as a function of time. However, AFSD is a dynamic process wherein temperatures are varying as a function of time throughout the thickness of the samples being deposited. As a result, the values of predicted grain size were monitored for various n values. It was observed that $n = 2.5$–2.9 provided the values between ~5–30 μm range (Table 3). These values were reasonably closer to the actually observed grain size distributions in the microstructures of the AFSD samples (Fig. 8 (b)–(d)). Such observations suggested that, due to the dynamic nature of the AFSD process, multiple grain growth exponents may have operated throughout the cross-section of the AFSD samples being fabricated. These estimates of grain sizes coupled with microscopy observations suggested that in a multi-layered/multi-pass thermomechanical process such as AFSD, the reheating can lead to commencement of the grain growth in the deposited recrystallized material. In addition, it was likely that some of the grains experienced preferential growth. Such a preferential grain growth could be attributed to the microscopic crystallographic texture evolution [64]. In light of this, EBSD analysis was performed on the samples as described in the following paragraphs.

To further probe into the microstructure and crystallographic texture evolution at micro level, EBSD scans were conducted on the AFSD samples in the *YZ* plane transverse to the deposition direction [20] and were compared with the EBSD data from the feed material (Fig. 9(a)–(d)). As observed during SEM examination (Fig. 8), the grain size was smaller for the AFSD samples processed with lower energy densities of 82 and 98 J/mm^2 compared to the feed material (IPF maps in Fig. 9(b) and (c)). With an increase in the total energy input to 116 J/mm^2 during AFSD, there was a shift in the grain size towards the coarser side (IPF map in Fig. 9(d)).

As a next step, to analyze the evolution of crystallographic texture, the texture plots for (0001), $(10\bar{1}0)$, and $(11\bar{2}0)$ were observed together with the HCP unit cell and standard 0001 pole figure [65] (Fig. 9(a)–(d)). The feed material wielded presence of a weak basal texture indicated by the diffuse intensity maxima at the north and south poles of the (0001) texture plot shown in Fig. 9(a). With the thermomechanical action of AFSD on the feed material, for the recrystallized deposited feed material corresponding to lowest energy density of 82 J/mm^2, the basal planes aligned mainly perpendicular to the *Z* axis ((0001) texture plot in Fig. 9(b)). Minor presence of basal planes perpendicular to the viewing *X* axis was observed. Furthermore, there was presence of weak prismatic texture indicated by the $(10\bar{1}0)$ and $(11\bar{2}0)$ texture plots (Fig. 9(b))). Similarly, the AFSD sample processed with total input energy of 98 J/mm^2 exhibited predominantly basal texture along with a slightly higher degree of prismatic texture (texture plots in Fig. 9(c))). The sample processed with highest total input energy of 116 J/mm^2 exhibited the strongest basal texture amongst all the AFSD samples with a high density of basal (0001) planes aligned perpendicular to the *Z* axis ((0001) texture plot in Fig. 9(d)). These findings were in agreement with the XRD spectra and the extracted intensity ratios which suggested that the prismatic planes were parallel to the *X* axis of the AFSD builds (Figs. 6 and 7).

In Mg based alloys, basal system ($\{0001\}$ and $\langle 11\bar{2}0\rangle$) is the closed pack slip system with lowest critical resolved shear stress (CRSS) [66]. The non basal slip systems, i.e., prismatic ($\{10\bar{1}0\}$ and $\langle 1\bar{2}10\rangle$) and pyramidal ($\{10\bar{1}1\}$ and $\langle 11\bar{2}3\rangle$ or $\{11\bar{2}2\}$ and $\langle \bar{1}\bar{1}23\rangle$) have approximately 100 times higher values of CRSS compared to the basal slip system [66–72]. As a result, the basal slip system dominates during deformation resulting in the basal texture evolution in the deformed Mg based materials [73–75]. The present analysis of EBSD and XRD also revealed predominantly basal texture within the AFSD samples (Figs. 6 and 7, and texture plots in Fig. 9). The intensity of basal texture increased as a function of total input energy. Furthermore, minor presence of prismatic texture was observed for samples processed with low total input energies (higher tool linear velocities). It has been reported that the prismatic slip system experiences relative increase in activity during the deformation in following conditions: i) presence of solute alloying elements leading to ease of prismatic slip activation due to reduction in Peierls stress [2,76,77]; ii) strain levels greater than 0.008 during the deformation process [78,79]; and iii) higher temperatures during the deformation process easing the thermal activation of the prismatic slip system [80,81]. In the present case, the AZ31B Mg alloy has aluminum and zinc in the solid solution of α-Mg. Moreover, typical strains during friction stir based processes have been reported to be in the range of −10 to 5 [53,82]. In addition, it is reported for FSP that the strain increases with an increase in the tool linear velocity [83]. Lastly, the peak temperatures reached during AFSD of the material were 0.75 to 0.8 times that of the liquidus temperature of 620 °C of AZ31B Mg [49] (Fig. 3). Therefore, the AFSD samples processed with higher tool linear velocities corresponding to 5.0 and 6.3 mm/s (total input energies of 82 and 98 J/mm^2) would have experienced activation of prismatic slip alongside the dominant basal slip resulting in a dominant basal and weak prismatic texture (texture plots in Fig. 9(b) and (c))). It is worth mentioning here that, currently in the present research group, an extensive study is ongoing with the aid of high resolution EBSD and site specific transmission electron microscopy to examine the spatial multi-scale evolution of microstructure and phase evolution which will be reported in a separate manuscript. In addition, parallel efforts are ongoing within the present research group to computationally predict the spatial-temporal evolution of residual stresses in the AFSD materials which drive the resultant microstructure and will be reported in the fu-

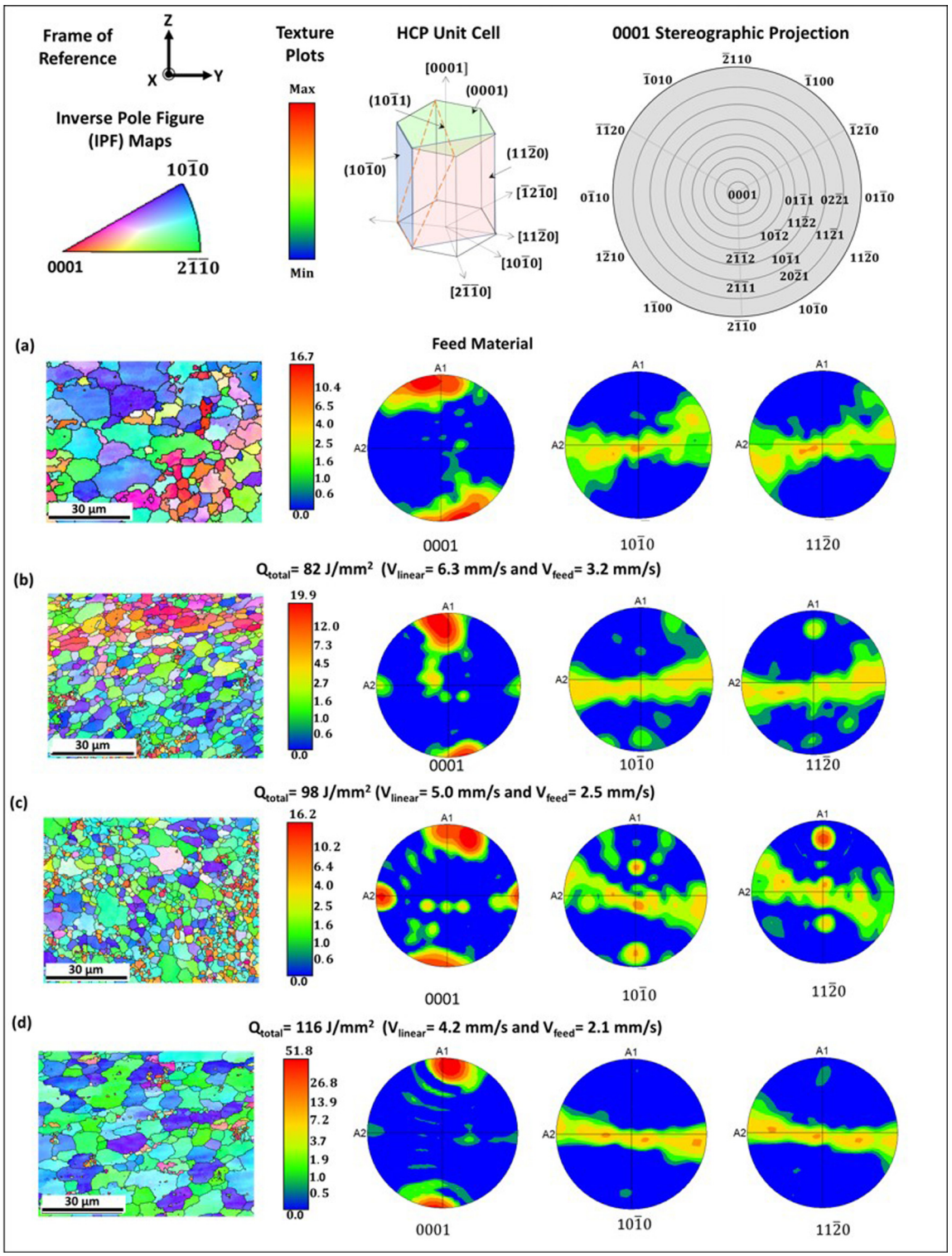

Fig. 9. Set of EBSD data depicting IPF maps, texture plots corresponding to 0001, $10\bar{1}0$, and $11\bar{2}0$ poles for (a) feed material and AFSD AZ31B Mg samples corresponding to (b) Q_{total} = 82 J/mm^2, (c) Q_{total} = 98 J/mm^2, and (d) Q_{total} = 116 J/mm^2. Schematic of hcp unit cell with various relevant planes and directions along with the standard 0001 stereographic projection are also shown.

ture. The intentions of the present preliminary work were to provide initial understanding of the AFSD process attributes and their effects on the evolution of microstructure in the material.

3.4. Hardness measurements

In order to realize the property response of the AFSD samples, the Vickers hardness measurements were conducted in

the *YZ* plane of the AFSD samples. Multiple indents were obtained throughout the cross-section at various locations of the deposits to probe the global and average values of hardness for each deposit. The hardness values were 56 ± 1.5, 58 ± 1.7, and 57 ± 3 Hv for the samples corresponding to the total energy inputs of 82, 98, and 116 J/mm^2 respectively. On the other hand, the feed material exhibited hardness of 53 ± 2 Hv indicating that there was a marginal increase in the hardness of AFSD samples attributed to the grain refinement observed for these samples (Figs. 8 and 9).

4. Conclusions

The present work explored solid state AM fabrication of AZ31B Mg alloy using AFSD technique. AFSD sample deposited with highest total energy input of 116 J/mm^2 exhibited a relatively rough surface (S_a = 19.5 μm) compared to samples deposited with lower energy densities of 98 and 82 J/mm^2 (R_a values of 13.7 and 9.8 μm respectively). All the AFSD samples indicated presence of α-Mg phase. The microstructure of AFSD samples consisted of equiaxed grains. The AFSD samples exhibited tighter grain size distributions when compared to the feed material. Majority of the grains were in the range of 0–10 μm for the AFSD samples with few larger grains in the range of 30–35 μm at the far end of the distribution. Based on Zener–Hollomon parameter related calculations, it appeared that the AFSD produced a recrystallized microstructure with fine grains in a freshly deposited material which was then subjected to growth due to reheating within the same layer and due to subsequently added layers. The feed material had a weak basal crystallographic texture. Application of AFSD on the feed material led to evolution of predominantly basal texture with basal planes aligned perpendicular to the *Z* axis of the builds. Vickers hardness of the AFSD samples was marginally higher (hardness = 56 ± 1.5, 58 ± 1.7, and 57 ± 3 Hv for samples corresponding to energy densities of 82, 98, and 116 J/mm^2) compared to the feed material (hardness = 53 ± 2 Hv). The present work provided a pathway for AM of AZ31B Mg alloy using novel solid state AFSD technique. It also laid out the framework for utilizing process attributes to realize processing-structure-property relationships in AFSD produced materials.

Acknowledgments

Authors acknowledge the infrastructure and support of Center for Agile and Adaptive Additive Manufacturing (CAAAM) funded through State of Texas Appropriation: 190405-105-805008-220 and Materials Research Facility (MRF) at the University of North Texas for access to microscopy and phase analysis facilities. Authors are thankful to Dr. Biswaranjan Dash and Dr. Priyanka Agrawal for their guidance on metallographic sample preparation.

References

[1] L. Commin, M. Dumont, J.-E. Masse, L. Barrallier, Friction stir welding of AZ31 magnesium alloy rolled sheets: influence of processing parameter, Acta Mater. 57 (2) (2009) 326–334.
[2] S.S. Joshi, M. Mohan, S. Seshan, S. Kumar, S. Suwas, Effect of addition of Al & Ca and heat treatment on the cast Mg-6Zn alloy, Mater. Sci. Forum 765 (2013) 33–37.
[3] J.S. Shrikant, Development of Cast Magnesium Alloys with Improved Strength, 2014 Master's thesis.
[4] M.K. Kulekci, Magnesium and its alloys applications in automotive industry, Int. J. Adv. Manuf. Technol. 39 (9–10) (2008) 851–865.
[5] B. Bagheri, M. Abbasi, A. Abdollahzadeh, S.E. Mirsalehi, Effect of second-phase particle size and presence of vibration on AZ91/SiC surface composite layer produced by FSP, Trans. Nonferrous Metals Soc. China 30 (4) (2020) 905–916.
[6] A. Abdollahzadeh, B. Bagheri, M. Abbasi, F. Sharifi, A.O. Moghaddam, Mechanical, wear and corrosion behaviors of AZ91/SiCcomposite layer fabricated by friction stir vibration processing, Surf. Topogr. 9 (3) (2021) 035038.
[7] E. Aghion, B. Bronfin, D. Eliezer, F. Von Buch, S. Schumann, H.E. Friedrich, The art of developing new magnesium alloys for high temperature applications, Mater. Sci. Forum 419 (2003) 407–418.
[8] T.-C. Wu, S.S. Joshi, Y.-H. Ho, M.V. Pantawane, S. Sinha, N.B. Dahotre, Microstructure and surface texture driven improvement in in-vitro response of laser surface processed AZ31b magnesium alloy, J. Magnes. Alloys 9 (2021) 1406–1418.
[9] N.B. Dahotre, S. Joshi, Machining of Bone and Hard Tissues, Springer, Cham, Switzerland, 2016.
[10] E. Aghion, B. Bronfin, Magnesium alloys development towards the 21st century, Mater. Sci. Forum 350 (2000) 19–30.
[11] A. Singh, S.P. Harimkar, Laser surface engineering of magnesium alloys: a review, JOM 64 (6) (2012) 716–733.
[12] R. Karunakaran, S. Ortgies, A. Tamayol, F. Bobaru, M.P. Sealy, Additive manufacturing of magnesium alloys, Bioact. Mater. 5 (1) (2020) 44–54.
[13] M.N. Jahangir, M.A.H. Mamun, M.P. Sealy, A review of additive manufacturing of magnesium alloys, in: AIP Conference Proceedings, vol. 1980, 2018, p. 030026.
[14] Y. Yang, C. Lu, L. Shen, Z. Zhao, S. Peng, C. Shuai, In-situ deposition of apatite layer to protect Mg-based composite fabricated via laser additive manufacturing, J. Magnes. Alloys (2021) (In press).
[15] F. Bär, L. Berger, L. Jauer, G. Kurtuldu, R. Schäublin, J.H. Schleifenbaum, J.F. Löffler, Laser additive manufacturing of biodegradable magnesium alloy WE43: a detailed microstructure analysis, Acta Biomater. 98 (2019) 36–49.
[16] T. Kurzynowski, A. Pawlak, I. Smolina, The potential of SLM technology for processing magnesium alloys in aerospace industry, Arch. Civ. Mech. Eng. 20 (1) (2020) 1–13.
[17] M. Gieseke, C. Noelke, S. Kaierle, V. Wesling, H. Haferkamp, Selective laser melting of magnesium and magnesium alloys, in: Magnesium Technology, Springer, 2013, pp. 65–68.
[18] J. Guo, Y. Zhou, C. Liu, Q. Wu, X. Chen, J. Lu, Wire arc additive manufacturing of AZ31 magnesium alloy: grain refinement by adjusting pulse frequency, Materials 9 (10) (2016) 823.
[19] D.A.M. Holguin, S. Han, N.P. Kim, Magnesium alloy 3D printing by wire and arc additive manufacturing (WAAM), MRS Adv. 3 (49) (2018) 2959–2964.
[20] S. Palanivel, P. Nelaturu, B. Glass, R. Mishra, Friction stir additive manufacturing for high structural performance through microstructural control in an Mg based WE43 alloy, Mater. Des. (1980–2015) 65 (2015) 934–952.
[21] Y.-H. Ho, S.S. Joshi, T.-C. Wu, C.-M. Hung, N.-J. Ho, N.B. Dahotre, In-vitro bio-corrosion behavior of friction stir additively manufactured AZ31B magnesium alloy-hydroxyapatite composites, Mater. Sci. Eng. 109 (2020) 110632.
[22] Y.-H. Ho, K. Man, S.S. Joshi, M.V. Pantawane, T.-C. Wu, Y. Yang, N.B. Dahotre, In-vitro biomineralization and biocompatibility of fric-

tion stir additively manufactured AZ31b magnesium alloy-hydroxyapatite composites, Bioact. Mater. 5 (4) (2020) 891–901.
[23] P. Angelo, R. Subramanian, Powder Metallurgy: Science, Technology and Applications, PHI Learning Pvt. Ltd., New Delhi, 2008.
[24] H.Z. Yu, R.S. Mishra, Additive friction stir deposition: a deformation processing route to metal additive manufacturing, Mater. Res. Lett. 9 (2) (2021) 71–83.
[25] Z.Y. Hang, M.E. Jones, G.W. Brady, R.J. Griffiths, D. Garcia, H.A. Rauch, C.D. Cox, N. Hardwick, Non-beam-based metal additive manufacturing enabled by additive friction stir deposition, Scr. Mater. 153 (2018) 122–130.
[26] P. Gradl, O. Mireles, N. Andrews, Intro to additive manufacturing for propulsion systems, in: AIAA Joint Propulsion Conference, 2018.
[27] U. Singh, M. Lohumi, H. Kumar, Additive manufacturing in wind energy systems: a review, in: Proceedings of International Conference in Mechanical and Energy Technology, Springer, 2020, pp. 757–766.
[28] D. Garcia, W.D. Hartley, H.A. Rauch, R.J. Griffiths, R. Wang, Z.J. Kong, Y. Zhu, Z.Y. Hang, In situ investigation into temperature evolution and heat generation during additive friction stir deposition: a comparative study of cu and al-Mg-Si, Addit. Manuf. 34 (2020) 101386.
[29] P. Agrawal, R.S. Haridas, S. Yadav, S. Thapliyal, S. Gaddam, R. Verma, R.S. Mishra, Processing-structure-property correlation in additive friction stir deposited Ti-6Al-4V alloy from recycled metal chips, Addit. Manuf. 47 (2021) 102259.
[30] M.E. Perry, H.A. Rauch, R.J. Griffiths, D. Garcia, J.M. Sietins, Y. Zhu, Y. Zhu, Z.Y. Hang, Tracing plastic deformation path and concurrent grain refinement during additive friction stir deposition, Materialia 18 (2021) 101159.
[31] R.J. Griffiths, M.E. Perry, J.M. Sietins, Y. Zhu, N. Hardwick, C.D. Cox, H.A. Rauch, Z.Y. Hang, A perspective on solid-state additive manufacturing of aluminum matrix composites using MELD, J. Mater. Eng. Perform. 28 (2) (2019) 648–656.
[32] P.M. Asiatico, The Applicability of Additive Friction Stir Deposition for Bridge Repair, Virginia Tech, 2021 Master's thesis.
[33] J. Dilip, G.J. Ram, Microstructure evolution in aluminum alloy AA 2014 during multi-layer friction deposition, Mater. Charact. 86 (2013) 146–151.
[34] J.R. Calvert, Microstructure and Mechanical Properties of WE43 Alloy Produced via Additive Friction Stir Technology, Virginia Tech, 2015 Master's thesis.
[35] A.N. Samant, B. Du, S.R. Paital, S. Kumar, N.B. Dahotre, Pulsed laser surface treatment of magnesium alloy: correlation between thermal model and experimental observations, J. Mater. Process. Technol. 209 (11) (2009) 5060–5067.
[36] G. Rapheal, S. Kumar, C. Blawert, N.B. Dahotre, Wear behavior of plasma electrolytic oxidation (PEO) and hybrid coatings of PEO and laser on MRI 230D magnesium alloy, Wear 271 (9–10) (2011) 1987–1997.
[37] S.R. Paital, A. Bhattacharya, M. Moncayo, Y.H. Ho, K. Mahdak, S. Nag, R. Banerjee, N.B. Dahotre, Improved corrosion and wear resistance of Mg alloys via laser surface modification of Al on AZ31B, Surf. Coat. Technol. 206 (8–9) (2012) 2308–2315.
[38] S. Santhanakrishnan, N. Kumar, N. Dendge, D. Choudhuri, S. Katakam, S. Palanivel, H. Vora, R. Banerjee, R. Mishra, N.B. Dahotre, Macro-and microstructural studies of laser-processed WE43 (Mg-Y-Nd) magnesium alloy, Metall. Mater. Trans. B 44 (5) (2013) 1190–1200.
[39] Y.-H. Ho, H.D. Vora, N.B. Dahotre, Laser surface modification of AZ31B Mg alloy for bio-wettability, J. Biomater. Appl. 29 (7) (2015) 915–928.
[40] T.-C. Wu, Y.-H. Ho, S.S. Joshi, R.S. Rajamure, N.B. Dahotre, Microstructure and corrosion behavior of laser surface-treated AZ31B Mg bio-implant material, Lasers Med. Sci. 32 (4) (2017) 797–803.
[41] J.Z. Lu, S.S. Joshi, M.V. Pantawane, Y.-H. Ho, T.-C. Wu, N.B. Dahotre, Optimization of biocompatibility in a laser surface treated Mg-AZ31B alloy, Mater. Sci. Eng. 105 (2019) 110028.
[42] N. Kalakuntla, N. Bhatia, S. Patel, S.S. Joshi, T.-C. Wu, Y.-H. Ho, N.B. Dahotre, Laser patterned hydroxyapatite surfaces on AZ31B magnesium alloy for consumable implant applications, Materialia 11 (2020) 100693.
[43] A. S. for TestingMaterials, ASTM E384-17: Standard Test Method for Microindentation Hardness of Materials, ASTM International, 2017.
[44] M. Riahi, H. Nazari, Analysis of transient temperature and residual thermal stresses in friction stir welding of aluminum alloy 6061-T6 via numerical simulation, Int. J. Adv. Manuf. Technol. 55 (1) (2011) 143–152.
[45] Z. Zhang, Z. Tan, J. Li, Y. Zu, W. Liu, J. Sha, Experimental and numerical studies of re-stirring and re-heating effects on mechanical properties in friction stir additive manufacturing, Int. J. Adv. Manuf. Technol. 104 (1) (2019) 767–784.
[46] C. Prosgolitis, S. Lambrakos, A. Zervaki, Phase-field modeling of nugget zone for a AZ31-Mg-alloy friction stir weld, J. Mater. Eng. Perform. 27 (10) (2018) 5102–5113.
[47] R. Nandan, G. Roy, T. Lienert, T. Debroy, Three-dimensional heat and material flow during friction stir welding of mild steel, Acta Mater. 55 (3) (2007) 883–895.
[48] S. Cui, Z. Chen, J. Robson, A model relating tool torque and its associated power and specific energy to rotation and forward speeds during friction stir welding/processing, Int. J. Mach. Tools Manuf. 50 (12) (2010) 1023–1030.
[49] A.K. Singh, P. Sahlot, M. Paliwal, A. Arora, Heat transfer modeling of dissimilar FSW of Al 6061/AZ31 using experimentally measured thermo-physical properties, Int. J. Adv. Manuf. Technol. 105 (1) (2019) 771–783.
[50] P. Podržaj, B. Jerman, D. Klobčar, Welding defects at friction stir welding, Metalurgija 54 (2) (2015) 387–389.
[51] S.P. Harimkar, N.B. Dahotre, Crystallographic and morphological textures in laser surface modified alumina ceramic, J. Appl. Phys. 100 (2) (2006) 024901.
[52] S. Ruppi, Deposition, microstructure and properties of texture-controlled CVD α-Al_2O_3 coatings, Int. J. Refract. Metals Hard Mater. 23 (4–6) (2005) 306–316.
[53] C. Chang, C. Lee, J. Huang, Relationship between grain size and Zener–Holloman parameter during friction stir processing in AZ31 Mg alloys, Scr. Mater. 51 (6) (2004) 509–514.
[54] B. Bagheri, M. Abbasi, A. Abdollahzadeh, A.H. Kokabi, A comparative study between friction stir processing and friction stir vibration processing to develop magnesium surface nanocomposites, Int. J. Min., Metall. Mater. 27 (8) (2020) 1133–1146.
[55] A. Kumar, N. Gotawala, S. Mishra, A. Shrivastava, Defects, microstructure and mechanical behaviour upon multi-pass friction stir processing of magnesium alloy with spiral tool path, CIRP J. Manuf. Sci. Technol. 32 (2021) 170–178.
[56] F. Yousefpour, R. Jamaati, H.J. Aval, Effect of traverse and rotational speeds on microstructure, texture, and mechanical properties of friction stir processed az91 alloy, Mater. Charact. 178 (2021) 111235.
[57] M. Abbasi, B. Bagheri, F. Sharifi, Simulation and experimental study of dynamic recrystallization process during friction stir vibration welding of magnesium alloys, Trans. Nonferrous Metals Soc. China 31 (9) (2021) 2626–2650.
[58] B. Bagheri, A. Abdollahzadeh, M. Abbasi, A.H. Kokabi, Effect of vibration on machining and mechanical properties of AZ91 alloy during FSP: modeling and experiments, Int. J. Mater. Form. 14 (4) (2021) 623–640.
[59] H. Mirzadeh, High strain rate superplasticity via friction stir processing (FSP): a review, Mater. Sci. Eng. 819 (2021) 141499.
[60] L. Ritti, T. Bhat, Design and numerical analysis of tool for FSP simulation of magnesium alloys, Mater. Today 46 (2021) 2489–2497.
[61] Q. Miao, L. Hu, X. Wang, E. Wang, Grain growth kinetics of a fine–grained AZ31 magnesium alloy produced by hot rolling, J. Alloys Compd. 493 (1–2) (2010) 87–90.
[62] P. Shewmon, Self-diffusion in magnesium single crystals, JOM 8 (8) (1956) 918–922.
[63] B.M. Darras, A model to predict the resulting grain size of friction–stir-processed AZ31 magnesium alloy, J. Mater. Eng. Perform. 21 (7) (2012) 1243–1248.

[64] M. Perez-Prado, O. Ruano, Texture evolution during annealing of magnesium AZ31 alloy, Scr. Mater. 46 (2) (2002) 149–155.
[65] Y. Luo, R. Qin, Surface energy and its anisotropy of hexagonal close–packed metals, Surf. Sci. 630 (2014) 195–201.
[66] R. Reed-Hill, W. Robertson, The crystallographic characteristics of fracture in magnesium single crystals, Acta Metall. 5 (12) (1957) 728–737.
[67] D. Poerschke, The Effects of Forging on the Microstructure and Tensile Properties of Magnesium Alloys AZ31 and ZK60, Technical Report, Published by Case Western Reserve University, Cleveland, OH, USA, 2009.
[68] J. Wu, S. Si, K. Takagi, T. Li, Y. Mine, K. Takashima, Y.L. Chiu, Study of basal $< a >$ and pyramidal $< c + a >$ slips in Mg-Y alloys using micro-pillar compression, Philos. Mag. 100 (11) (2020) 1454–1475.
[69] S. Agnew, M. Yoo, C. Tome, Application of texture simulation to understanding mechanical behavior of Mg and solid solution alloys containing Li or Y, Acta Mater. 49 (20) (2001) 4277–4289.
[70] X. Lou, M. Li, R. Boger, S. Agnew, R. Wagoner, Hardening evolution of AZ31B Mg sheet, Int. J. Plast. 23 (1) (2007) 44–86.
[71] R. Reed-Hill, W. Robertson, Additional modes of deformation twinning in magnesium, Acta Metall. 5 (12) (1957) 717–727.
[72] S. Hui, Z. Chu, H. Wang, Y. Li, L. Ma, C. Xue, Mechanism of secondary deformation of extruded AZ31 magnesium alloy by viscoplastic self-consistent model, Adv. Mater. Sci. Eng. 2020 (2020) 8791720.
[73] Y. Qiao, X. Wang, Z. Liu, E. Wang, Effect of temperature on microstructures, texture and mechanical properties of hot rolled pure Mg sheets, Mater. Sci. Eng. 568 (2013) 202–205.
[74] F.-c. Liu, Z.-y. Ma, M.-j. Tan, Facilitating basal slip to increase deformation ability in Mg–Mn–Ce alloy by textural reconstruction using friction stir processing, Metall. Mater. Trans. A 44 (8) (2013) 3947–3960.
[75] C. Lee, J. Huang, X. Du, Improvement of yield stress of friction–stirred Mg–Al–Zn alloys by subsequent compression, Scr. Mater. 56 (10) (2007) 875–878.
[76] A. Akhtar, E. Teghtsoonian, Solid solution strengthening of magnesium single crystals—I alloying behaviour in basal slip, Acta Metall. 17 (11) (1969) 1339–1349.
[77] A. Akhtar, E. Teghtsoonian, Solid solution strengthening of magnesium single crystals—II the effect of solute on the ease of prismatic slip, Acta Metall. 17 (11) (1969) 1351–1356.
[78] M.A. Shabana, J.J. Bhattacharyya, M. Niewczas, S.R. Agnew, Thermally activated nature of basal and prismatic slip in Mg and its alloys, in: Magnesium Technology, Springer International Publishing, 2021, pp. 53–60.
[79] Y. Li, P. Hou, Z. Wu, Z. Feng, Y. Ren, H. Choo, Dynamic recrystallization of a wrought magnesium alloy: grain size and texture maps and their application for mechanical behavior predictions, Mater. Des. 202 (2021) 109562.
[80] S. Razavi, D. Foley, I. Karaman, K. Hartwig, O. Duygulu, L. Kecskes, S. Mathaudhu, V. Hammond, Effect of grain size on prismatic slip in Mg–3Al–1Zn alloy, Scr. Mater. 67 (5) (2012) 439–442.
[81] S. Biswas, S.S. Dhinwal, S. Suwas, Room-temperature equal channel angular extrusion of pure magnesium, Acta Mater. 58 (9) (2010) 3247–3261.
[82] A. Arora, Z. Zhang, A. De, T. DebRoy, Strains and strain rates during friction stir welding, Scr. Mater. 61 (9) (2009) 863–866.
[83] Z. Zhang, H. Zhang, Numerical studies on the effect of transverse speed in friction stir welding, Mater. Des. 30 (3) (2009) 900–907.